2021-12-16

A large West Antarctic Ice Sheet explains early Neogene sea-level amplitude

Marschalek, JW

10.1038/s41586-021-04148-0
Nature
Springer Science and Business Media LLC

A Large West Antarctic Ice Sheet Explains Early Neogene Sea-Level Amplitude

J.W. Marschalek[1], L. Zurli[2], F. Talarico[2], T. van de Flierdt[1], P. Vermeesch[3], A. Carter[4], F. Beny[5], V. Bout-Roumazeilles[5], F. Sangiorgi[6], S. Hemming[7], L.F. Peréz[8,9,10], F. Colleoni[9], J. Prebble[11], T.E. van Peer[12], M. Perotti[2], I. Browne[13], A. Shevenell[13], D.K. Kulhanek[14], R. Levy[8,11], D. Harwood[15], N.B. Sullivan[16], S.R. Meyers[16], E. Griffith[17], C.-D. Hillenbrand[10], E. Gasson[18], M.J. Siegert[1,19], K. Licht[20], B. Keisling[7], G. Kuhn[21], J. Dodd[22], C. Boshuis[6] , L. De Santis[9], R.M. McKay[8], and the Expedition 374 scientists.

[1]Department of Earth Science and Engineering, Imperial College London, Exhibition Road, London, SW7 2AZ, UK; j.marschalek18@imperial.ac.uk

[2]Department of Physical, Earth and Environmental Sciences, University of Siena, via Laterina 8, 53100 Siena, Italy

[3]Department of Earth Sciences, University College London, UK

[4]Department of Earth and Planetary Sciences, Birkbeck, University of London, UK

[5]Laboratoire d'Océanologie et de Géosciences, UMR 8187 CNRS/Univ Lille/ULCO, 8 Cité scientifique, F-59655 Villeneuve d'Ascq, France.

[6]Marine Palynology and Paleoceanography, Department of Earth Sciences, University of Utrecht, The Netherlands

[7]Lamont-Doherty Earth Observatory of Columbia University Palisades, New York, USA

[8]Antarctic Research Centre, Victoria University of Wellington, Wellington, New Zealand

[9]Geophysics Division, Istituto Nazionale di Oceanografia e di Geofisica Sperimentale, Trieste, Italy

[10]British Antarctic Survey, High Cross, Madingley Road, Cambridge, UK

[11]GNS Science, Lower Hutt, New Zealand.

[12]National Oceanography Centre Southampton, University of Southampton Waterfront Campus, Southampton, UK

[13]College of Marine Science, University of South Florida, St. Petersburg, FL, USA

[14]International Ocean Discovery Program, Texas A&M University, TX, USA

[15]Department of Earth and Atmospheric Sciences, University of Nebraska-Lincoln, Lincoln, NE 68588-0340, USA

[16]Department of Geoscience, University of Wisconsin-Madison, Madison, WI 53706, USA

[17]School of Earth Sciences, Ohio State University, Columbus, OH 43210, USA

[18]School of Geographical Sciences, University Road, University of Bristol, Bristol, BS8 1SS, UK.

[19]Grantham Institute, Imperial College London, Exhibition Road, South Kensington, London SW7 2AZ, UK

[20]Department of Earth Sciences, Indiana University Purdue University Indianapolis, Indianapolis, USA

[21]Alfred Wegener Institute, Helmholtz Centre for Polar and Marine Research, 27568 Bremerhaven, Germany

[22]Department of Geology, Northern Illinois University, DeKalb, Illinois 60115, USA

Early Neogene sea-level oscillations of approximately 40-60 m estimated from far-field records[1,2,3] have been interpreted as requiring the loss of virtually all Antarctic ice during peak interglacials[2]. This contrasts with ice-sheet model experiments suggesting most terrestrial ice in East Antarctica was retained even during the warmest intervals of the middle Miocene[4,5]. Data and model outputs can be reconciled if a large West Antarctic Ice Sheet (WAIS) expanded across the outer continental shelf during the early Miocene, accounting for the maximum ice-sheet volumes. Here, we provide geochemical and petrographic evidence from International Ocean Discovery Programme (IODP) Site U1521 showing that early Miocene glacimarine sediments (~17.72-17.40 Ma) in the central Ross Sea were clearly derived from West Antarctica. Complimentary seismic, lithological and palynological data reveal that grounded ice was intermittently proximal to the site. This is the earliest geological evidence for WAIS expansion across most of the Ross Sea shelf. Rapid deposition of nearly 190 m of sediment at Site U1521 in ~320 kyr implies unusually fast glacial erosion of West Antarctica. This interval therefore represents a key step in the genesis of a marine-based WAIS and a tipping point in Antarctic ice-sheet evolution.

Introduction

Reconstructing past changes to Antarctica's ice sheets helps inform predictions of the continent's future contribution to sea-level rise[6,7]. Drilling efforts around Antarctica since the 1970s have begun to reveal the Cenozoic evolution of Antarctic glaciation[8,9,10,11], but fundamental steps in the development of the ice sheets remain poorly constrained. One key uncertainty is the timing of West Antarctic Ice Sheet (WAIS) expansion across the outer continental shelf. Early work on benthic

53 oxygen isotope records and Antarctic abyssal plain sedimentary records suggested WAIS formation
54 did not occur until the late Miocene or early Pliocene[12,13]. However, more recent drilling from the
55 Antarctic margin[11,14,15] and ice-sheet modelling studies[4,5,16] have raised the possibility that ice-sheet
56 expansions into the marine realm could have occurred in the early Miocene or even earlier,
57 facilitated by a subaerial West Antarctic topography[17,18].

58 Without widespread WAIS expansions across the continental shelf in the Early Neogene, maximum
59 ice volumes are low enough that global sea-level fluctuations of ~40-60 m seen in far-field
60 stratigraphic records[1] and oxygen isotope-derived ice volume estimates[2,3] require the near complete
61 loss of the East Antarctic Ice Sheet (EAIS) during the warmest middle Miocene periods[2]. This is
62 incompatible with current ice-sheet model outputs, which show retention of most terrestrial East
63 Antarctic ice even during the warmest feasible middle Miocene environmental conditions[4]. This is
64 mainly due to hysteresis effects driven by height-mass balance feedbacks, where the presence of the
65 ice sheet means ice can be retained following warming beyond the point which the ice sheet would
66 be able to form in[4,19].

67 Marine sediments, deposited on the continental shelf of the Ross Sea, can reveal whether the WAIS
68 expanded across the continental shelf, but existing geological records are hampered by poor
69 recovery, unconformities and/or close proximity to East Antarctica[9,10,11]. Seismic data show
70 significant volumes of early Miocene glacimarine sediment deposited around the West Antarctic
71 margin[20,21,22,23], but these data require age and physical property constraints from drilling. They also
72 lack the resolution to conclusively differentiate between sediment supply from continental-scale ice-
73 sheet expansion and local ice caps on (paleo)topographic highs[22,23]. Consequently, WAIS grounding
74 across the shelf is only clear in seismic data after the cooling of the Miocene Climate Transition (~14
75 Ma)[24,25]; it remains uncertain whether there were earlier WAIS expansions across the Ross Sea shelf.

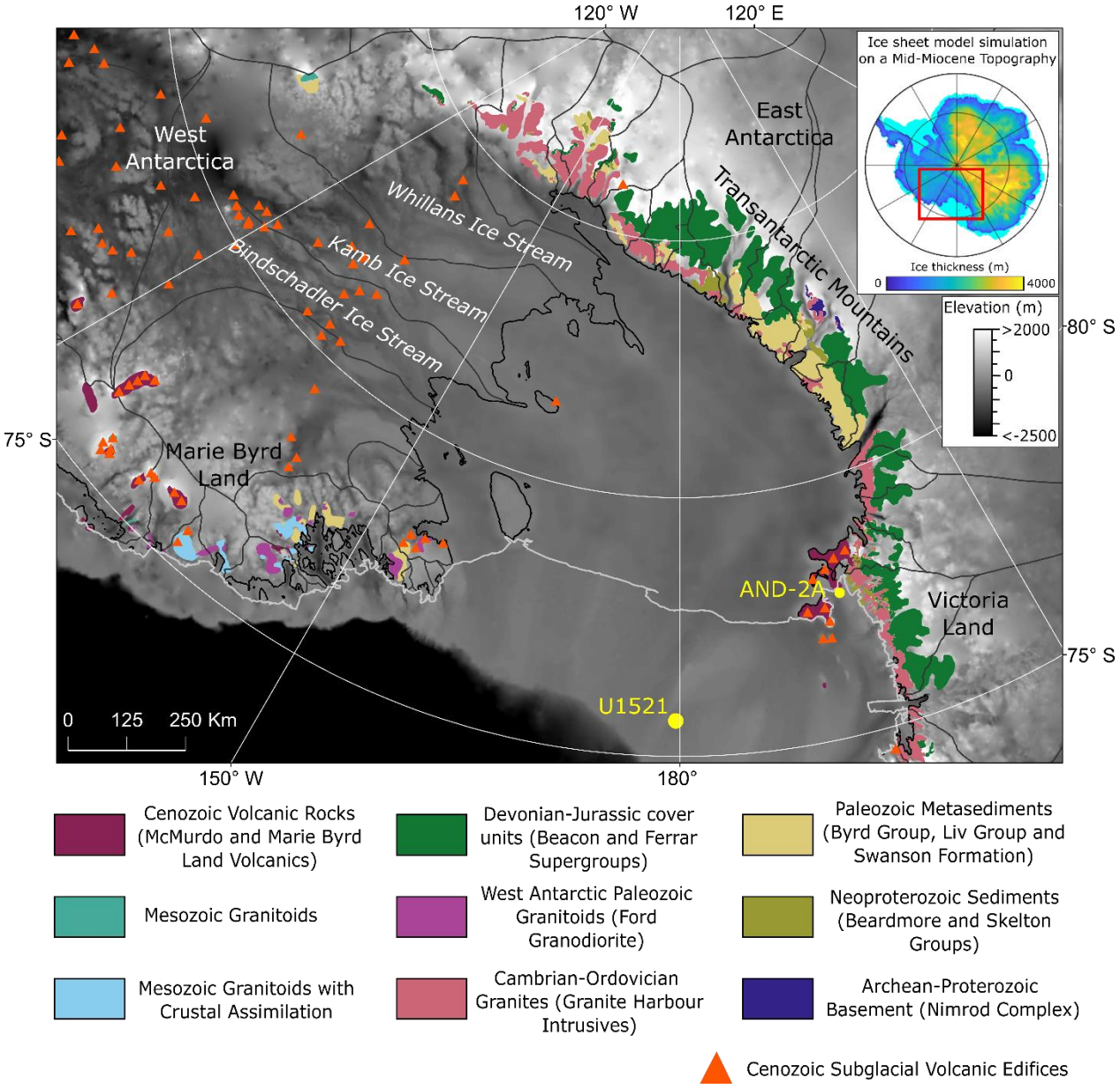

Figure 1. *Map of the Ross Sea region showing the outcropping regional geology[26] overlain on the BedMachine Antarctica V1 modern bed topography[27]. IODP Site U1521 is located on the outer continental shelf of the central Ross Sea. Key locations referenced in the text are labelled, including the ANDRILL 2A (AND-2A) drill site. The white dashed line indicates the boundary between East and West Antarctic lithosphere[28]. Orange triangles show Cenozoic subglacial volcanic edifices detected based on morphological characteristics, gravity anomalies and magnetic anomalies[29]. The inset shows an ice-sheet model run using a 'cold' climate and a mid-Miocene topography. Provenance indicators from Sequence 2 sediments at Site U1521 are broadly consistent with an ice sheet similar to or exceeding the extent of the model output pictured, which was simulated on a Mid-Miocene topography with a 'cold' orbit and 280 ppm CO_2 climate[4].*

IODP Site U1521 and Provenance Approach

IODP Site U1521 (75°41.0’ S, 179°40.3’ W) was drilled to 650.1 metres below sea floor (mbsf) in the Pennell Basin on the outer continental shelf of the Ross Sea in 562 m water depth (Fig. 1). The site was strategically located in a region that ice-sheet models indicate is one of the last sectors in Antarctica where ice grounds during glacial maxima, making it an ideal location to assess the timing of past maxima in ice-sheet extent and WAIS expansions onto the outer continental shelf[4,16,30]. The sediments from base of the hole up to 209.17 mbsf constitute an expanded early Miocene sequence (~18 to ~16.3 Ma; see Supplement for details on the age model) with 73% recovery. Individual sequences (1-4) are differentiated based on unconformities in the chronostratigraphic framework and divided further (A/B) based on major lithological boundaries. These sediments provide a unique window for detailed analysis of ice-sheet behaviour immediately before the Miocene Climate Optimum (MCO, ~17-15 Ma; Fig. 2; Fig. S1; Table S1).

The sediments below 209.17 mbsf at Site U1521 are predominantly muddy to sandy diamictites, often interbedded with thin laminae and beds of mudstone (see detailed lithological descriptions in the Supplement)[30]. Palynological counts on 23 samples (see Supplement and Table S3) revealed sparse palynomorphs in Sequence 1 and 4A, common reworked dinoflagellate cysts in Sequence 2 and evidence for high biological productivity in Sequence 3B (Fig. S8). Thus, the lithological and palaeontological data from Sequences 1, 2, 3A and 4A suggest a predominantly ice-proximal glacimarine (and potentially subglacial) setting, while data from Sequence 3B suggest an ice-distal setting. Notably, the ~190 m Sequence 2 succession, containing a high proportion of reworked dinoflagellate cysts, was deposited rapidly (~0.6 mm $year^{-1}$) within a ~320 kyr interval spanning ~17.72-17.40 Ma (Fig. S1).

Through comparison to terrestrial rock outcrops, the marine sediments at Site U1521 were traced back to their source region. A differing geological history of the rocks beneath the EAIS and WAIS (Fig. 1) gives the sediment eroded by each ice sheet a distinct geochemical, petrological and

mineralogical composition, allowing expansions from each ice sheet to be distinguished. We applied multiple sediment provenance proxies to avoid bias towards, or omission of, any lithologies[31]. Specifically, we analysed the detrital fine fraction of 37 samples for neodymium (Nd) and strontium (Sr) isotope compositions (<63 µm) and 23 samples for clay mineralogy (<2 µm). Eight of these samples were processed for U-Pb dating of detrital zircons (<300 µm) and five for $^{40}Ar/^{39}Ar$ dating of detrital hornblende grains (150-300 µm). Additionally, the petrography of 15,740 clasts >2 mm was identified continuously down-core (Fig. S7).

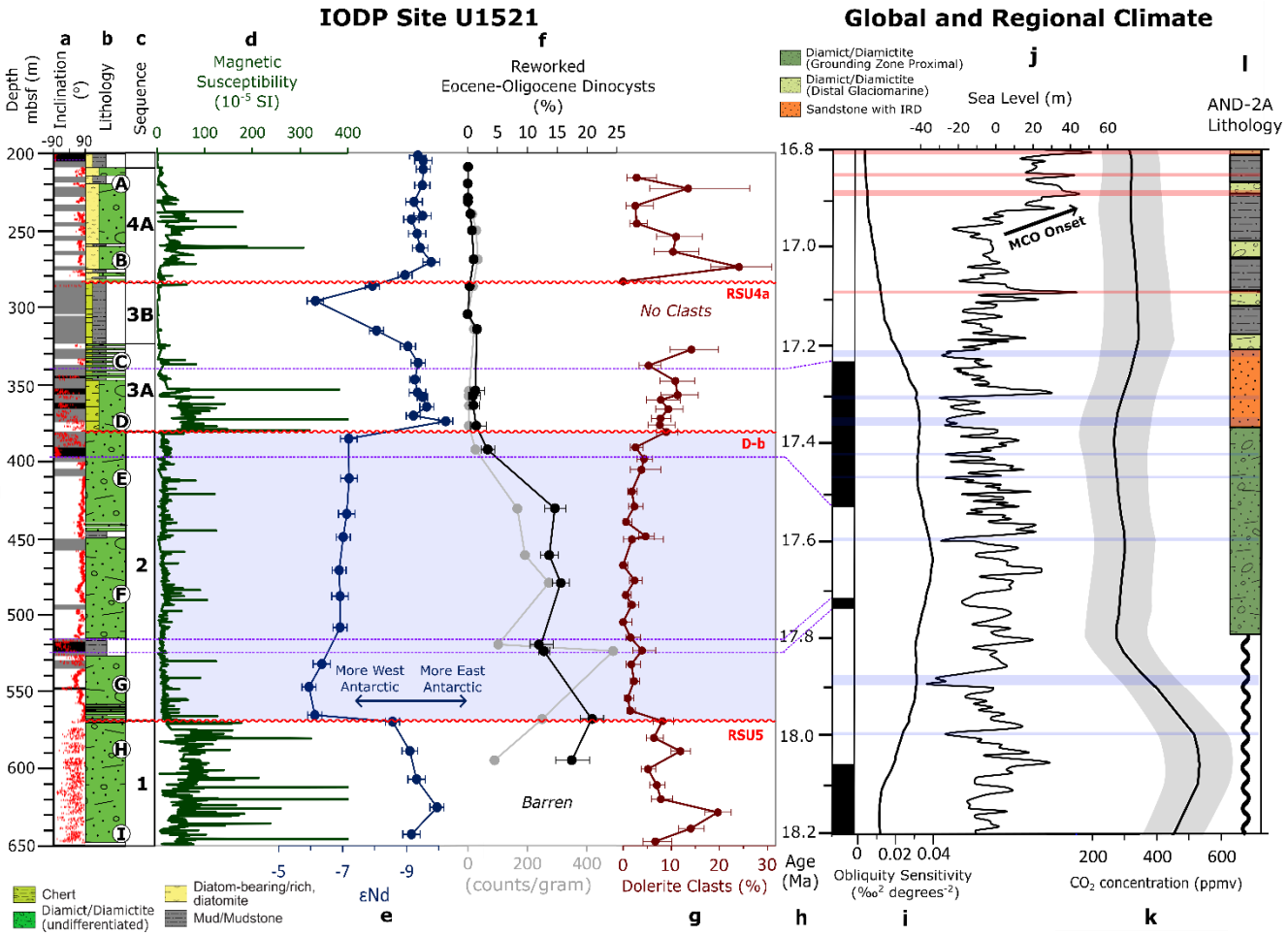

Figure 2. *Selected provenance proxies from IODP Site U1521 compared to early Miocene climate records. The blue shaded section (Sequence 2) highlights the interval with sediments of predominantly West Antarctic provenance. The depth of Ross Sea Unconformity (RSU) 4a and 5 and seismic surface D-b are indicated in red[23]. a) Site U1521 inclination data after 20 nT demagnetisation (red points)[30] and polarity interpretation*

(white = reverse polarity, black = normal polarity, grey = no interpretation). b) Site U1521 lithostratigraphy. c) Chronostratigraphic sequences. The circled letters between b) and c) show the depths of the zircon U-Pb samples shown in Figure 3. d) Magnetic susceptibility measured on the whole core[30]. e) Neodymium isotope data (error bars are 2 S.D. external reproducibility). f) Abundance of Eocene-Oligocene dinocysts as a percentage (black) and concentration (grey). g) Dolerite clast abundance. Errors shown in f) and g) are 95% confidence intervals[32]. Magnetostratigraphic tie points between the polarity interpretations from shipboard data (a)[30] and geomagnetic polarity timescale (h)[33] are marked by purple dashed lines. i) Obliquity sensitivity, indicating the strength of obliquity in the $\delta^{18}O$ record relative to the theoretical strength of obliquity forcing. This has been interpreted as representing the presence of marine-based Antarctic ice[15]. j) Sea-level record based on an oxygen isotope splice[2]. Red and blue shaded intervals indicate pronounced sea-level highstands (>40 m) and lowstands (<-20 m), respectively. MCO = Miocene Climatic Optimum. k) Compilation of CO_2 proxy records with a LOESS smoothing (shaded region indicates 1 sigma error), including all available proxies (phytoplankton, paleosols, boron isotopes, leaf gas exchange, stomatal frequencies and the $\delta^{13}C$ value of terrestrial C3 plant remains). References for the CO_2 compilation are provided in the methods section. k) Simplified lithological log from the AND-2A record, with diamictites differentiated based on a grounding-zone proximal vs distal glacimarine depositional setting[11,15].

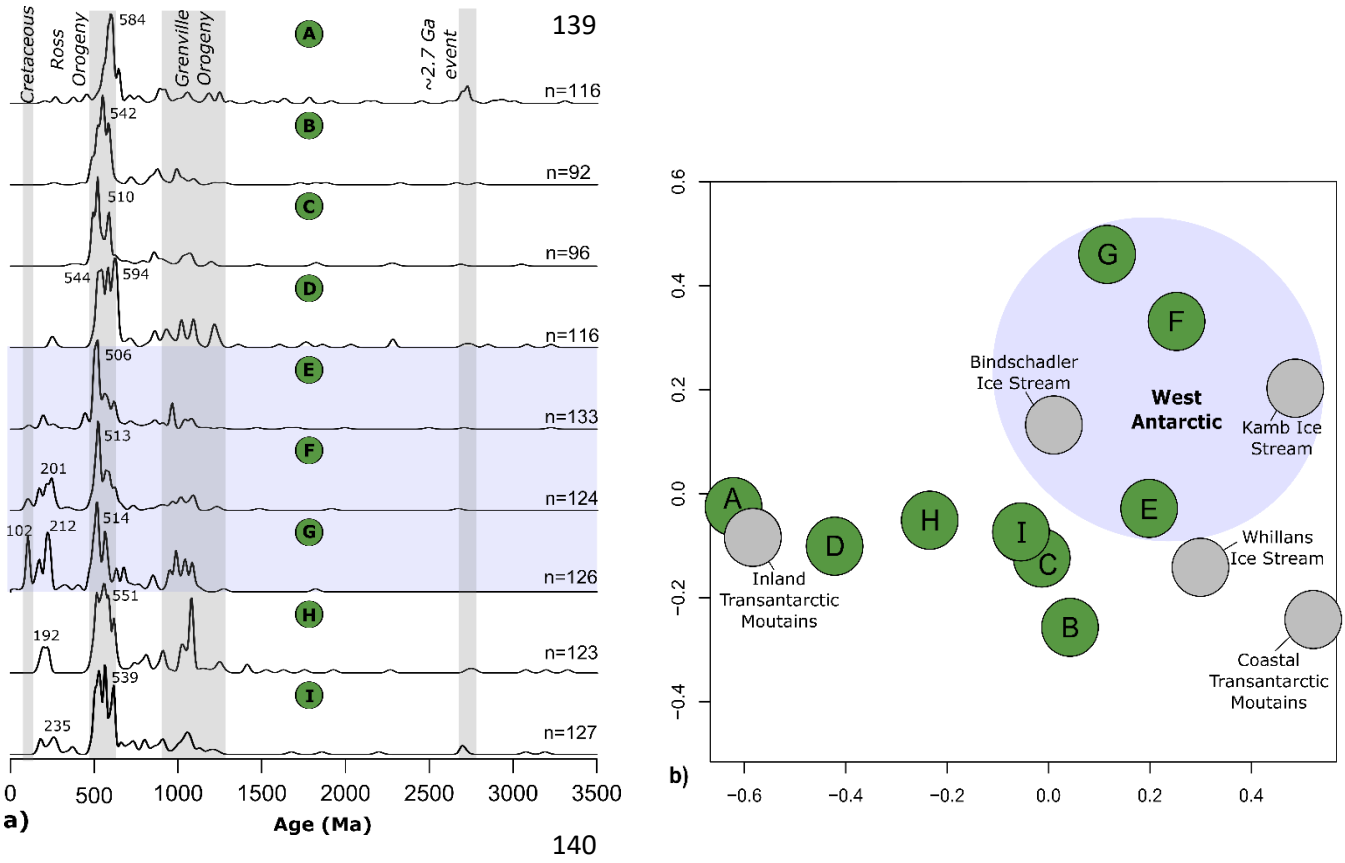

Figure 3. *a) Detrital zircon U-Pb ages displayed as kernel density estimates (KDEs). When present, large Ross Orogeny (~600-500 Ma), Triassic (~240-190 Ma) and Cretaceous (~100 Ma) age peaks are labelled. The age ranges of the Ross Orogeny, Grenville Orogeny and a ~2.7 Ga event recorded in Ross Sea sedimentary strata are illustrated using grey-shaded bars. Descending in depth, the samples midpoints are 220.23, 270.03, 335.72, 373.58, 410.82, 487.40, 546.55, 588.00 and 642.21 mbsf, as shown on the lithological log in Figure 2. The same data are displayed in b) as a multi-dimensional scaling (MDS) plot calculated using the Kolmogorov–Smirnov statistic[34]. Stress (a measurement of the goodness of fit between the disparities and the fitted distances[34]) = 0.072. A MDS plot visualises the degree of similarity between each sample, with any two points plotting closer if they are more similar. The axis scales are dimensionless and have no physical meaning. Samples from Site U1521 (shaded green) are compared to previously published zircon U-Pb data (shaded grey) from Kamb, Whillans and Bindschadler ice streams in West Antarctica, as well as Transantarctic Mountain moraines from more inland and more coastal regions[35,36,37]. The KDEs and region of the MDS plot interpreted as having a West Antarctic provenance are shaded in blue, consistent with Figure 2.*

Note that although Whillans Ice Stream drains the WAIS, it is excluded from the blue shaded area as its close proximity to the Transantarctic Mountains leads to a provenance indistinguishable from East Antarctica[36].

Evidence for Early Miocene WAIS Growth

At Site U1521, detrital ε_{Nd} values are consistently more radiogenic (higher) in Sequence 2 compared to the sediments above and below (Fig. 2), implying a contribution from a more radiogenic end member. This end member can be traced to beneath the WAIS; the ε_{Nd} values, ranging between -7.2 and -5.9, are in good agreement with measurements of late quaternary diamicts from the eastern Ross Sea shelf, adjacent to West Antarctica[38]. Here, the radiogenic end member is hypothesised to be the Cenozoic alkali volcanic rocks of Marie Byrd Land in West Antarctica[38] (Fig. S3). Subaerial outcrops of the Marie Byrd Land volcanic province are limited, but magnetic and gravity anomalies associated with subglacial cone-shaped structures indicate the presence of numerous subglacial volcanoes (Fig. 1)[29]. These are likely to be the more radiogenic end member contributing to Sequence 2. Conversely, the less radiogenic (lower) ε_{Nd} values seen in adjacent sediments, ranging between -10.2 and -8.6, reflect a mixture of lithologies present in the (East Antarctic) Transantarctic Mountains and fall within the range of late quaternary Ross Sea tills of Transantarctic Mountain provenance (Fig. S3, S6)[38,39]. These less radiogenic sediments also show higher and more variable magnetic susceptibility (Fig. 2)[30]. The patterns seen in the ε_{Nd} data are broadly mirrored by detrital Sr isotope compositions (Fig. S8).

Single-grain geochronology/thermochronology and clast petrography can provide more detailed insights into specific source terranes. In the Transantarctic Mountains, Precambrian rocks were affected by the pervasive Ross Orogeny (615-470 Ma), which was accompanied by extensive intrusive felsic magmatism (see Supplementary Information)[40]. Zircon age populations from Sequences 1, 3A and 4A show a strong peak towards the earlier part of the Ross Orogeny (595 to 535 Ma) and a 6 to 21% population of Archaean and Paleoproterozoic (>1600 Ma) zircon grains

178 (Figs. 1, 3). These features, together with a lack of grains younger than 250 Ma, resemble moraines
179 in the Transantarctic Mountains[35,36,37]. Clasts in sequences 1, 3A and 4A also correlate with rocks in
180 the Transantarctic Mountains, with lithologies including common felsic granitoids and meta-
181 greywackes alongside rarer limestones, marbles and sandstones (Fig. S7)[40]. Although a relatively
182 minor component, dolerite clasts are found throughout Sequences 1, 3A and 4A (Fig. 2g) and these
183 are unique to the Jurassic Ferrar Group, which outcrops in the Transantarctic Mountains (Fig. 1).
184 Furthermore, rare *Protohaploxypinus* pollen, a distinctive component of the Permian Beacon
185 Supergroup sediments from the Transantarctic Mountains, are observed in Sequence 3A[41]. Overall,
186 the sediments comprising Sequences 1, 3A and 4A at Site U1521 are predominantly sourced from
187 erosion of the Transantarctic Mountains in East Antarctica.

188 In contrast, Sequence 2, characterized by the highest ε_{Nd} values, contains Cretaceous (~100 Ma)
189 zircon U-Pb ages (n = 16; Fig. S5, Fig. 3a). Such ages are indicative of a West Antarctic provenance,
190 as they are presently only found beneath modern Siple Coast ice streams including Kamb Ice Stream
191 and those closer to Marie Byrd Land[36,42]. The age spectra from Sequence 2 share many other features
192 with data from the Siple Coast ice streams, including a broad Triassic (~240-190 Ma) age peak, few
193 pre-Mesoproterozoic zircons (<5 % of grains) and a young (~515-505 Ma) Ross Orogeny peak (Fig.
194 3)[36]. Detrital hornblende $^{40}Ar/^{39}Ar$ ages from Sequence 2 further corroborate a West Antarctic
195 provenance. Unlike zircon grains, which can survive multiple sedimentary cycles, hornblende grains
196 are less resistant to weathering. The absence of Grenvillian (~1100-900 Ma) ages in the Sequence 2
197 hornblende sample (Fig. S5) suggests a West Antarctic provenance, as Grenville-age rocks are absent
198 there[43]. The scarcity of Ferrar Group dolerite clasts, common in the Transantarctic Mountains, is also
199 consistent with a West Antarctic provenance (Figs. 1, 2). Additionally, Sequence 2 contains evidence
200 for recycling of older marine detritus, most likely from the Early Cenozoic rift-fill strata that exist in
201 the eastern Ross Sea region of the West Antarctic Rift System[21]. This is inferred from the dominance
202 of reworked Eocene-Oligocene species in the diatom and spore-pollen assemblages[29], alongside the

common (13-21%) reworked Eocene-Oligocene marine dinocysts, which are rare (<1.5%) in younger sediments (Fig. S8).

Finally, the high abundance of smectite - up to 58% at the bottom of Sequence 2 (Fig. S7, S9) – provides further evidence of a West Antarctic provenance; Quaternary sediments in the eastern Ross Sea (adjacent to West Antarctica) have a similarly high smectite content[44]. In addition to this evidence for a provenance shift, smectite content significantly declines up-section within Sequence 2. This falling contribution is accompanied by a rise in basalt clast abundance (Fig. S9), which is unexpected given that smectite is considered a weathering product of basalt and volcanic rocks. This trend of increasing basalt clast abundances and falling basalt weathering product (i.e. smectite) is consistent with the removal of a more weathered regolith layer, followed by erosion of progressively more pristine, less weathered, continental detritus. The ~17.72 to 17.40 Ma Sequence 2 interval could therefore have seen the first advance of grounded ice over these areas of West Antarctica for an extended period.

Further evidence for WAIS expansion across the shelf can be found in seismic data[23]. The sediment package deposited at Site U1521 between ~17.72 and 17.40 Ma can be traced across the Ross Sea continental shelf and contains widespread progradational wedges and high relief morainal banks[20,21,23]. Given the abundant occurrence of diamictites at Site U1521 and the glacial features distinguished in the seismic dataset, marine-terminating ice was clearly present during this interval. The seismic package is also thicker towards the eastern Ross Sea (i.e. West Antarctica)[23]. Taken together, the seismic data, high deposition rate, common reworked marine microfossils and provenance data revealing transport of large volumes of West Antarctic detritus as far west as the Pennell Basin in the central Ross Sea, all indicate that the early Miocene WAIS must have intermittently extended across most of the outer continental shelf.

Our data therefore show that WAIS expansions across the Ross Sea continental shelf date back to at least ~17.72 Ma, prior to the Miocene Climatic Transition (~14 Ma) and significantly earlier than

228 previously suggested[12,13,23,24,45]. This ~17.72 to 17.40 Ma WAIS advance coincides with an interval
229 of high obliquity sensitivity (Fig. 2i), supporting the use of this metric as a proxy for enhanced ice-
230 sheet sensitivity to ocean dynamics and thus marine-based ice advance[15].

231 **Birth of a Marine-Based WAIS**

232 The mean erosion rate for the Ross Sea sector of the WAIS between ~17.72 and 17.40 Ma can be
233 estimated using the volume of the corresponding seismic package east of Site U1521 (see
234 supplementary methods)[23]. Assuming that, at the time of deposition, the area of the Ross Sea
235 drainage sector of the WAIS was approximately the same as today, the inferred sediment volume
236 requires a mean catchment erosion of approximately 90 (-30/+50) m in ~320 kyr (Table S2). The
237 erosion rate in this interval (~0.275 mm a^{-1}) exceeds the long-term mean rate calculated for this part
238 of the WAIS between 23 and 14 Ma (0.012 mm a^{-1})[18] by a factor of more than 20. This highlights the
239 ~17.72 to 17.40 Ma period as one of unusually rapid erosion, with erosion rates comparable to
240 modern subpolar to temperate glacial catchments[46]. Transporting this large volume of subglacially
241 eroded debris quickly to the WAIS margin required abundant meltwater at the ice-sheet bed[47], as
242 well as fast-flowing ice streams that extended into marine settings where broad deposition could take
243 place. This required sufficiently cool ocean temperatures permitting the advance of marine-based ice,
244 yet warm enough atmospheric conditions to provide sufficient precipitation to drive dynamic ice
245 flow and enhanced basal erosion[4].

246 Since most of West Antarctica, apart from Marie Byrd Land, was thermally subsiding throughout the
247 Miocene[18], the high erosion rate at ~17.72 to 17.40 Ma is unlikely to have been driven by tectonic
248 uplift. The eroded sediments therefore reflect a rapid lowering of the terrestrial West Antarctic
249 hinterland and infilling of the Ross Sea basins, although we acknowledge our data cannot directly
250 constrain topographic change. This erosive event occurred at a time when topographic
251 reconstructions show there was a transition from a terrestrial West Antarctica (at 23 Ma) to a largely

sub-marine West Antarctica (at 14 Ma)[18]. The timing and large volume of sediment deposited in Sequence 2 suggests this interval must therefore record a critical step in this transition of the WAIS from a largely terrestrial ice-sheet to one that was primarily marine-based (i.e. mainly grounded below sea level). This critical change to West Antarctic topography occurred almost immediately prior to the significant changes to Antarctic cryosphere and climate seen during the MCO[2,11]. This suggests subglacial erosion drove changes in ice-sheet behaviour as, after ~17.40 Ma, a greater submarine area in central West Antarctica would have made the mass-balance control of the WAIS more sensitive to external drivers such as sea-level and oceanic forcing[5,16]. We propose that ice retreat at the onset of the MCO may be partially attributable to the crossing of this topographic tipping point and that Sequence 2 records the birth of a marine-based WAIS. We date this event to well before 14 Ma, the time slice at which topographic reconstructions first show a largely sub-marine West Antarctica[18].

Sea-Level Reconciliation

Grounded ice flowing from West Antarctica was close to Site U1521 towards the end of the early Miocene. We therefore validate recent modelling studies suggesting that an ice-sheet nucleating on a partially terrestrial West Antarctica could expand extensively into the marine realm under early Miocene climatic and paleotopographic conditions[4,5,16]. Our data are consistent with an ice extent similar to, or exceeding, the largest modelled early to middle Miocene Antarctic ice sheets (Fig. 1), equivalent to up to ~80 m of global average sea level depending on the reconstructed topography used[4,5,16]. This evidence for an expanded WAIS, containing approximately 14-15 m SLE[4,16], implies the loss of nearly all terrestrial East Antarctic ice during the warmest periods of the Miocene is not required; far-field sea-level amplitudes of ~40-60 m[1,2,3] allow for terrestrial ice to remain, consistent with modelled hysteresis effects[4]. By providing the earliest conclusive evidence for a large marine-

based WAIS, our data also dispel the long-held notion that a WAIS, able to impact global eustacy and climate, was not present until ~14 Ma, or even later[12,13,45].

References

1. Kominz, M. A. et al. Miocene relative sea level on the New Jersey shallow continental shelf and coastal plain derived from one-dimensional backstripping: A case for both eustasy and epeirogeny. *Geosphere* **12**, 1437-1456 (2016).
2. Miller, K. G. et al. Cenozoic sea-level and cryospheric evolution from deep-sea geochemical and continental margin records. *Science advances* **6**, p. eaaz1346 (2020).
3. Pekar, S. F., & DeConto, R. M. High-resolution ice-volume estimates for the early Miocene: Evidence for a dynamic ice sheet in Antarctica. *Palaeogeogr., Palaeoclimatol., Palaeoecol.* **231**, 101-109 (2006).
4. Gasson, E., DeConto, R. M., Pollard, D. & Levy, R. H. Dynamic Antarctic ice sheet during the early to mid-Miocene. *Proc. Natl. Acad. Sci. USA* **113**, 3459–3464 (2016).
5. Paxman, G. J., Gasson, E. G., Jamieson, S. S., Bentley, M. J., & Ferraccioli, F. Long-Term Increase in Antarctic Ice Sheet Vulnerability Driven by Bed Topography Evolution. *Geophysical Research Letters* **47**, e2020GL090003 (2020).
6. Masson-Delmotte, V. et al. Information from paleoclimate archives. *Climate change* 383–464 (2013).
7. Kennicutt, M. C. et al. A roadmap for Antarctic and Southern Ocean science for the next two decades and beyond. *Antarctic Science* **27**, 3-18 (2014).
8. Kennett, J. P. Cenozoic evolution of Antarctic glaciation, the circum-Antarctic Ocean, and their impact on global paleoceanography. *Journal of Geophysical Research* **82**, 3843-3860 (1977).
9. Barrett, P. J. Characteristics of pebbles from Cenozoic marine glacial sediments in the Ross Sea (DSDP Sites 270–274) and the South Indian Ocean (Site 268). In *Initial Reports of the Deep-Sea Drilling Project* **28**, 769-784 (1975).

10. Passchier, S., & Krissek, L. A. Oligocene–Miocene Antarctic continental weathering record and paleoclimatic implications, Cape Roberts drilling project, Ross Sea, Antarctica. *Palaeogeogr., Palaeoclimatol., Palaeoecol.* **260**, 30-40 (2008).
11. Levy, R. et al. Antarctic ice sheet sensitivity to atmospheric CO2 variations in the early to mid-Miocene. *Proceedings of the National Academy of Sciences* **113**, 3453-3458 (2016).
12. Zachos, J., Pagani, M., Sloan, L., Thomas, E., & Billups, K. Trends, rhythms, and aberrations in global climate 65 Ma to present. *Science* **292**, 686-693 (2001).
13. Kennett, J.P., and Barker, P.F. Latest Cretaceous to Cenozoic climate and oceanographic developments in the Weddell Sea, Antarctica: an ocean-drilling perspective. *Proc. Ocean Drill. Program Sci. Results* **113**, 937–960 (1990). doi:10.2973/odp.proc.sr.113.195.1990
14. Hauptvogel, D. W., & Passchier, S. Early–Middle Miocene (17–14 Ma) Antarctic ice dynamics reconstructed from the heavy mineral provenance in the AND-2A drill core, Ross Sea, Antarctica. *Global and Planetary Change* **82**, 38-50 (2012).
15. Levy, R. H. et al. Antarctic ice-sheet sensitivity to obliquity forcing enhanced through ocean connections. *Nature Geoscience* **12**, 132-137 (2019).
16. Colleoni, F. et al. Past continental shelf evolution increased Antarctic ice sheet sensitivity to climatic conditions. *Scientific reports* **8**, 1-12 (2018).
17. Wilson, D. S. et al. Antarctic topography at the Eocene-Oligocene boundary, *Palaeogeogr. Palaeoclimatol. Palaeoecol.* **335-336**, 24–34 (2012). doi:10.1016/j.palaeo.2011.05.028.
18. Paxman, G. J., Jamieson, S. S., Hochmuth, K., Gohl, K., Bentley, M. J., Leitchenkov, G., & Ferraccioli, F. Reconstructions of Antarctic topography since the Eocene–Oligocene boundary. *Palaeogeogr., Palaeoclimatol., Palaeoecol.* **535** (2019).
19. Gasson, E. G., & Keisling, B. A. The Antarctic Ice Sheet: A Paleoclimate Modelling Perspective. *Oceanography* **33**, 90-100 (2020).

20. Anderson, J. B., & Bartek, L. R. Cenozoic glacial history of the Ross Sea revealed by intermediate resolution seismic reflection data combined with drill site information. *The Antarctic Paleoenvironment: A Perspective on Global Change: Part One* **56**, 231-264 (1992).
21. De Santis, L., Anderson, J. B., Brancolini, G., & Zayatz, I. Seismic record of late Oligocene through Miocene glaciation on the central and eastern continental shelf of the Ross Sea. *Geology and Seismic Stratigraphy of the Antarctic Margin* **68**, 235-260 (1995).
22. Gohl, K. et al. Seismic stratigraphic record of the Amundsen Sea Embayment shelf from pre-glacial to recent times: Evidence for a dynamic West Antarctic Ice Sheet. *Marine Geology* **344**, 115-131 (2013).
23. Pérez, L.F. et al. Early-middle Miocene ice sheet dynamics in the Ross Sea embayment: results from integrated core-log-seismic interpretation. *GSA Bulletin* (2021).
24. Bart, P. J. Were West Antarctic ice sheet grounding events in the Ross Sea a consequence of East Antarctic ice sheet expansion during the middle Miocene? *Earth and Planetary Science Letters* **216**, 93-107 (2003).
25. Chow, J. M., & Bart, P. J. West Antarctic Ice Sheet grounding events on the Ross Sea outer continental shelf during the middle Miocene. *Palaeogeogr., Palaeoclimatol., Palaeoecol.* **198**, 169-186 (2003).
26. Cox S.C., Smith Lyttle B. and the GeoMAP team. *SCAR GeoMAP dataset*. GNS Science, Lower Hutt, New Zealand. Release v.201907 (2019). https://doi.org/10.21420/7SH7-6K05
27. Morlighem, M. *et al.* Deep glacial troughs and stabilizing ridges unveiled beneath the margins of the Antarctic ice sheet. *Nat. Geosci.* **13,** 132–137 (2020). https://doi.org/10.1038/s41561-019-0510-8
28. Tinto, K.J. *et al.* Ross Ice Shelf response to climate driven by the tectonic imprint on seafloor bathymetry. *Nat. Geosci.* **12,** 441–449 (2019). https://doi.org/10.1038/s41561-019-0370-2

29. van Wyck de Vries, M., Bingham, R. G., & Hein, A. S. A new volcanic province: an inventory of subglacial volcanoes in West Antarctica. *Geological Society, London, Special Publications* **461**, SP461. 467 (2017).
30. McKay, R., De Santis, L., Kulhanek, D. K., and the Expedition 374 Science Party. Ross Sea West Antarctic Ice Sheet History. College Station, Texas, International Ocean Discovery Program, *Proceedings of the International Ocean Discovery Program* (2019).
31. Licht, K. J., & Hemming, S. R. Analysis of Antarctic glacigenic sediment provenance through geochemical and petrologic applications. *Quaternary Science Reviews* **164**, 1-24 (2017).
32. Vermeesch, P. Statistical models for point-counting data. *Earth and Planetary Science Letters* **501**, 112-118 (2018).
33. Ogg, J. Geomagnetic Polarity Time Scale. In *Geologic Time Scale 2020* (eds. Gradstein, F. M. *et al.*) 159–192 (Elsevier, 2020).
34. Vermeesch, P. Multi-sample comparison of detrital age distributions. *Chemical Geology* **341**, 140-146 (2013).
35. Licht, K. J., & Palmer, E. F. Erosion and transport by Byrd Glacier, Antarctica during the last glacial maximum. *Quaternary Science Reviews* **62**, 32-48 (2013).
36. Licht, K. J., Hennessy, A. J., & Welke, B. M. The U-Pb detrital zircon signature of West Antarctic ice stream tills in the Ross embayment, with implications for Last Glacial Maximum ice flow reconstructions. *Antarctic Science* **26**, 687-697 (2014).
37. Bader, N. A., Licht, K. J., Kaplan, M. R., Kassab, C., & Winckler, G. East Antarctic ice sheet stability recorded in a high-elevation ice-cored moraine. *Quaternary Science Reviews* **159**, 88-102 (2017).

38. Farmer, G. L., Licht, K., Swope, R. J., & Andrews, J. Isotopic constraints on the provenance of fine-grained sediment in LGM tills from the Ross Embayment, Antarctica. *Earth and Planetary Science Letters* **249**, 90-107 (2006).
39. Farmer, G. L., & Licht, K. J. Generation and fate of glacial sediments in the central Transantarctic Mountains based on radiogenic isotopes and implications for reconstructing past ice dynamics. *Quaternary Science Reviews* **150**, 98-109 (2016).
40. Goodge, J. W. Geological and tectonic evolution of the Transantarctic Mountains, from ancient craton to recent enigma. *Gondwana Research* **80**, 50-122 (2020).
41. Kyle, R.A. & Schopf, J.M. Permian and Triassic palynostratigraphy of the Victoria Group, Transantarctic Mountains: in Craddock, C., ed., *Antarctic geoscience*: Madison, University of Wisconsin Press, International Union of Geological Sciences, Series B-4, 649–659 (1982).
42. Perotti, M., Andreucci, B., Talarico, F., Zattin, M., & Langone, A. Multianalytical provenance analysis of Eastern Ross Sea LGM till sediments (Antarctica): Petrography, geochronology, and thermochronology detrital data. *Geochemistry, Geophysics, Geosystems* **18**, 2275-2304 (2017).
43. Jordan, T. A., Riley, T. R., & Siddoway, C. S. The geological history and evolution of West Antarctica. *Nature Reviews Earth & Environment* **1**, 1-17 (2020).
44. Balshaw-Biddle, K. M. Antarctic glacial chronology reflected in the Oligocene through Pliocene sedimentary section in the Ross Sea (Rice University, 1981).
45. Westerhold, T. et al. An astronomically dated record of Earth's climate and its predictability over the last 66 million years. *Science* **369**, 1383-1387 (2020)
46. Koppes, M. et al. Observed latitudinal variations in erosion as a function of glacier dynamics. *Nature* **526**, 100–103 (2015).
47. Alley, R. B., Cuffey, K. M., & Zoet, L. K. Glacial erosion: status and outlook. *Annals of Glaciology* **60**, 1-13 (2019).

Methods

Neodymium and Strontium Isotopes

Samples were disaggregated and wet sieved to isolate the <63 μm fraction, which was then dried down at 60°C. This size fraction represents the bulk composition, as samarium and neodymium are incorporated in equal proportions into most rock-forming minerals meaning grain-size sorting is not likely to impact results[48,49]. However, the Rb-Sr system is subject to elemental fractionation during weathering and grain-size sorting, which can influence $^{87}Sr/^{86}Sr$ ratios (see 'Provenance Changes within Sequence 2' section in supplement). To remove authigenic Fe-Mn oxyhydroxide phases, samples were leached in a mixture of 0.05 M hydroxylamine hydrochloride, 15% acetic acid, and 0.03 M EDTA at a pH of 450. A carbonate removal step was not included due to the very low carbonate content[30]. Leached sediment was dried, homogenised, and 50 mg aliquots were digested on a hotplate in concentrated HF (2 mL), $HClO_4$ (0.8 mL) and HNO_3 (1 mL) for three to five days, with a subsequent 6 M HCl step. The Nd was isolated from the sample matrix using a cation exchange resin (AG50W-X8, 200-400 μm mesh) and HCl in increasing molarity, followed by a low molarity HCl Ln-Spec resin procedure (50–100 μm mesh). The sample matrix from the cation exchange step was dried down, taken up in HNO_3, then loaded onto Eichrom Sr Spec resin to wash down the matrix and elute the Sr[51].

Neodymium isotopes were measured in the MAGIC laboratories at Imperial College London on a Nu high resolution multi-collector inductively coupled plasma mass spectrometer (HR MC-ICP-MS). To account for instrumental mass bias, isotope ratios were corrected using an exponential law and a $^{146}Nd/^{144}Nd$ ratio of 0.7219. Although negligible, interference of ^{144}Sm on ^{144}Nd was corrected for. Bracketing standards were used to correct measured $^{143}Nd/^{144}Nd$ ratios to the commonly used JNdi-1 value of 0.512115[52]. USGS BCR-2 rock standard was processed alongside all samples and yielded $^{143}Nd/^{144}Nd$ ratios consistently within error of the published ratio of 0.512638 ± 0.000015[53]. Full procedural blanks for Nd ranged from 7 to 30 pg (n = 6). $^{143}Nd/^{144}Nd$ ratios are expressed using

epsilon notation (ε_{Nd}), which denotes the deviation of a measured ratio from the modern Chondritic Uniform Reservoir (0.512638)[54] in parts per 10,000.

Strontium isotopes were measured in the MAGIC laboratories at Imperial College London on a TIMS (Thermal Ionisation Mass Spectrometer). 10% of the sample was loaded in 1 µL of 6M HCl onto degassed tungsten filaments with 1 µL of $TaCl_5$ activator. The measured $^{87}Sr/^{86}Sr$ ratios were corrected for instrumental mass bias using an exponential law and an $^{88}Sr/^{86}Sr$ ratio of 8.375. Interference of ^{87}Rb was corrected for using an $^{87}Rb/^{85}Rb$ ratio of 0.386. Analyses of the NIST 987 standard reference material were completed every four unknowns, yielding a mean of 0.710290 ± 0.000041 (2SD, n = 36). Samples were corrected to the published value of 0.710252 ± 0.000013[53]. The relatively poor reproducibility for our NIST 987 runs was due to technical issues, but is still more than sufficient for interpreting sample results, which change in the 3rd to 4th digit. Accuracy of results was confirmed using rock standard USGS BCR-2, processed with every batch of samples, which yielded $^{87}Sr/^{86}Sr$ ratios of 0.705010 ± 0.00029 (2SD, n = 18). This is well within error of the published value of 0.705013 ± 0.00010[53].

Detrital Zircon U-Pb Dating

To ensure there were enough grains for statistical analysis, samples were taken over 40 cm of core. Samples were disaggregated, dried and sieved at 300 µm. Zircons from the <300 µm fraction were concentrated using standard gravity settling and magnetic separation techniques. Samples were then mounted in resin, polished and analysed using an Agilent 7900 laser ablation inductively-coupled plasma mass spectrometer (LA-ICP-MS) with a 25-35 µm pit diameter in the London Geochronology Centre at University College London. Approximately 150 grains resembling zircons were randomly selected for analysis from each sample. Plešovice zircon[55] was used as a primary standard to correct for instrumental mass bias and depth-dependent inter-element fractionation. Approximate U and Th concentrations were calculated by comparison with NIST 612 glass[56].

Data reduction of the time-resolved mass spectrometer data was performed using GLITTER 4.5[57]. Ages younger than 1100 Ma were calculated using the $^{206}Pb/^{238}U$ ratio whilst older grains used the $^{207}Pb/^{206}Pb$ ratio. Data were filtered to exclude non-zircons based on zirconium concentrations ($>10^6$ counts per second) and a -5/+15% discordance threshold was applied. This yielded at least 92 grains per sample, giving a 95% confidence that any age populations comprising more than 7% of the sample will be measured[58]. GJ1 zircon[59] was used as a secondary standard to verify accuracy of the data. Repeat analyses using zircons with and without existing ablation pits were made to check sample reproducibility; these agreed within the uncertainties associated with random sampling. Final data were processed and visualised using the R package IsoplotR[60].

Clast Petrography

The gravel fraction (>2 mm) was characterized in continuum along the core, between 648.17 and 209.17 mbsf. Clasts exposed in the cut surface of the archive half core were measured, logged and described on the basis of macroscopic features (e.g. shape, colour, texture). Logging aimed to identify the distribution and variation of the gravel-size clasts along the core length. Clast logging followed the methodologies applied to the ANDRILL and CRP records; on the basis of macroscopic features, clasts were grouped into seven main lithological groups: igneous rocks, quartz fragments, dolerites, volcanic rocks, metamorphic rocks, sedimentary rocks and sedimentary intraclasts[61,62,63,64]. Data processing involved counting the occurrence of each lithological group over each 10 cm core interval. The total number of clasts in each core was then divided by the core length to normalize the clast abundance, and the number of clasts for each lithological group was summarized for each core (Fig. S7). To highlight the along-core variation in dolerite and volcanic clasts - two of the most indicative lithologies for provenance constraint - the number of these clasts was divided by the total number of clasts in each core (Fig. S7). A total of 73 pebble to cobble-sized clasts were sampled for

469 petrographic analysis, of which the most representative of each lithological group were analysed
470 using standard petrographic methods with polarized light microscopy.

471 *Palynology*

472 Sample processing was performed at Utrecht University, following standard techniques of the
473 Laboratory of Palaeobotany and Palynology. Samples were oven-dried and weighed (~15 g dry
474 weight sediment each). One *Lycopodium clavatum* tablet with a known amount of marker spores was
475 added for quantification of palynomorph abundances[65].

476 Samples were treated with 10% HCl (Hydrochloric acid) and cold 38% HF (Hydrofluoric acid), then
477 sieved over a 10 μm mesh with occasional mild ultrasonic treatment. To avoid any potential
478 processing-related preservation bias, no oxidation or acetolysis was carried out. The processed
479 residue was transferred to microscope slides using glycerine jelly as a mounting medium, and 2
480 slides were analysed per sample at 400× magnification. Slides were examined for detailed marine
481 (dinoflagellate cysts, acritarchs and other aquatic palynomorphs) and screening-level terrestrial
482 (pollen and spore) analysis at Utrecht University, with a subsequent detailed analysis for terrestrial
483 palynomorphs on a sub-set of seven samples undertaken at GNS Science. Of the 23 palynological
484 samples analysed for dinocysts, two contained < 60 dinocysts (Sequence 1; 594.48 mbsf and
485 Sequence 2; 567.75 mbsf) and one was almost barren (yielding only 12 *in situ* dinocysts, Sequence
486 3A; 374.9 mbsf). The almost barren sample is excluded from all plots. The two low abundance
487 samples are included in our dataset; however, because of the low dinocyst yield, careful
488 interpretation is required. Samples between 594.48 and 567.75 mbsf and below 594.48 mbsf (cores
489 65R, 67R, 69R and 71R) were also checked, but yielded few dinocyst specimens. Those present
490 comprised of fragments of mostly reworked dinocysts.

491 Pollen and spore identification followed taxonomic compilations[66,67], augmented by key Antarctic
492 literature[68,69,70]. For pollen and spores, scanning continued until an entire cover slide was completed,

493 or a 100 count reached. Results are presented as specimens/gram, and percentage of all terrestrial
494 palynomorphs. Dinocysts were identified based on a taxonomical index[71] and informally and
495 formally described species in the literature[72,73,74,75]. Dinocyst percentages were calculated based on
496 the total *in situ* dinocysts counted, excluding reworked specimens (Table S3). The percentages of
497 other palynomorph groups such as brackish and freshwater algae (*Cymatiosphaera* spp. and
498 *Pediastrum* spp.) and reworked dinocysts were calculated using the total palynomorphs counted (Fig.
499 2; Fig. S8). *In situ* dinocyst and terrestrial palynomorph absolute abundance (specimens/g dry
500 weight, Table S3) and the absolute abundance of the other palynomorph groups were calculated by
501 counting the amount of *Lycopodium clavatum* spores encountered, following the equation of
502 Benninghoff (1962)[76].

503 Protoperidinioid (P) dinocysts are mostly represented by the genera *Brigantedinium*, *Lejeunecysta*,
504 and *Selenopemphix*. Gonyaulacoid (G) dinocysts mostly include *Batiacasphaera* spp.,
505 *Operculodinium* spp. and *Spiniferites* spp. Protoperidinioid cyst percentages (Heterotrophic % in Fig.
506 S8; Table S3) and percentages of the most common species (*Brigantedinium* spp. *Lejeunecysta* spp.,
507 *Selenopemphix* spp. and *Selenopemphix antarctica*) were calculated to identify productivity trends
508 and/or the presence of sea ice (see Supplementary Information). P dinocysts are likely produced by
509 heterotrophic dinoflagellates[77] and, at present, dominate the assemblages in Antarctic sediments in
510 areas with high nutrients and/or (year-round) sea-ice covered areas. At present, samples in quasi
511 perennial sea-ice covered areas are dominated by *Selenopemphix antarctica* (~75%), with abundant
512 *Brigantedinium* spp. and rare occurrence of other species[78,79,80]. G cysts are generally produced by
513 phototrophic dinoflagellates. *Operculodinium* spp. is the most abundant, has species representatives
514 among the extant cysts and has been selected to represent temperate-warm conditions. At present, it
515 is almost exclusively found in temperate areas of the Southern Ocean, north of the Subantarctic
516 Front[78] and never occurs in the circum-Antarctic sediments, while it was found common to abundant

517 in other Antarctic warm Miocene records[81,82]. Reworked dinocysts include Eocene and Oligocene
518 taxa (mostly *Vozzhennikovia* spp., but also few *Spinidinium* spp. and *Enneadocysta diktyostila*).

519 *Paleo CO_2 Compilation*

520 Proxy estimates of atmospheric CO_2 concentrations (Fig. 2) were obtained from the compilations on
521 the websites paleo-co2.org and p-co2.org. Proxies include the $\delta^{13}C$ of marine phhtoplankton[83,84,85],
522 the $\delta^{13}C$ of paleosols[86,87], boron isotope ($\delta^{11}B$) proxies[88,89,90,91], leaf gas-exchange[92], stomatal
523 frequencies[93] and the $\delta^{13}C$ of terrestrial C3 plants[94]. An assessment of the validity of different proxies
524 is beyond the scope of this paper, so all available proxies were included. The complied data are
525 presented as a LOESS-smoothed curve through the data using the 'loess' function in R. The shaded
526 region indicates 1 sigma error.

527 **Methods References**

528 48. Goldstein, S. L., & Hemming, S. R. Long-lived isotopic tracers in oceanography,
529 paleoceanography, and ice-sheet dynamics. *Treatise on geochemistry* **6**, 625 (2003).
530 49. Garçon, M., Chauvel, C., France-Lanord, C., Huyghe, P., & Lavé, J. (2013). Continental
531 sedimentary processes decouple Nd and Hf isotopes. *Geochimica et Cosmochimica*
532 *Acta*, *121*, 177-195.
533 50. Gutjahr, M., Frank, M., Stirling, C. H., Klemm, V., Van de Flierdt, T., & Halliday, A. N.
534 Reliable extraction of a deepwater trace metal isotope signal from Fe–Mn oxyhydroxide
535 coatings of marine sediments. *Chemical Geology* **242,** 351-370 (2007).
536 51. Simões Pereira, P. et al. Geochemical fingerprints of glacially eroded bedrock from West
537 Antarctica: Detrital thermochronology, radiogenic isotope systematics and trace element
538 geochemistry in Late Holocene glacial-marine sediments. *Earth-Science Reviews* **182**, 204-
539 232 (2018).
540 52. Tanaka, T. et al. JNdi-1: a neodymium isotopic reference in consistency with LaJolla
541 neodymium. *Chem. Geol*. **168**, 279–281 (2000).
542 53. Weis, D. et al. High-precision isotopic characterization of USGS reference materials by
543 TIMS and MC-ICP-MS. *Geochem. Geophys. Geosyst*. **7**, Q08006 (2006).
544 54. Jacobsen, S. B. & Wasserburg, G. J. *Earth planet. Sci. Lett.* **50**, 139 (1980).
545 55. Sláma, J. et al. Plešovice zircon—a new natural reference material for U–Pb and Hf isotopic
546 microanalysis. *Chemical Geology* **249**, 1-35 (2008).
547 56. Pearce, N. J. et al. A compilation of new and published major and trace element data for
548 NIST SRM 610 and NIST SRM 612 glass reference materials. *Geostandards newsletter* **21**,
549 115-144 (1997).
550 57. Griffin, W. L. GLITTER: data reduction software for laser ablation ICP-MS. *Laser Ablation*
551 *ICP-MS in the Earth Sciences: Current practices and outstanding issues*, 308-311 (2008).

552 58. Vermeesch, P. How many grains are needed for a provenance study? *Earth and Planetary*
553 *Science Letters* **224**, 441-451 (2004).
554 59. Jackson, S. E., Pearson, N. J., Griffin, W. L., & Belousova, E. A. The application of laser
555 ablation-inductively coupled plasma-mass spectrometry to in situ U–Pb zircon
556 geochronology. *Chemical geology* **211**, 47-69 (2004).
557 60. Vermeesch, P. IsoplotR: A free and open toolbox for geochronology. *Geoscience Frontiers* **9**,
558 1479-1493 (2018).
559 61. Talarico F. & Sandroni S. Petrography, Mineral Chemistry and Provenance of Basement
560 Clasts in the CRP-1 Drillcore (Victoria Land Basin, Antarctica). *Terra Antartica* **5**, 601-610
561 (1998).
562 62. Talarico, F., Sandroni, S., Provenance signature of the Antarctic Ice Sheets in the Ross
563 Embayment during the Late Miocene to Early Pliocene: the ANDRILL AND-1B core record.
564 *Global and Planetary Change* **69**, 103–123 (2009).
565 63. Talarico F., Sandroni S., Fielding C.R. & Atkins C. Variability, Petrography and Provenance
566 of Basement Clasts from CRP-2/2A Drillcore (Victoria Land Basin, Ross Sea, Antarctica).
567 *Terra Antarctica* **7**, 529-544 (2000).
568 64. Sandroni, S., and Talarico, F. M. Petrography and provenance of basement clasts and clast
569 variability in CRP-3 drillcore (Victoria Land Basin, Antarctica), *Terra Antarctica* **8**, 449-467
570 (2001).
571 65. Wood, G. D., Gabriel, A. M. & Lawson, J. C. In: Palynology: Principles and Applications
572 (Eds Jansonius, J. & McGregor, D. C.) 29–50. American Association of Stratigraphic
573 Palynologists Foundation, Dallas, TX (1996).
574 66. Raine, J.I., Mildenhall, D.C., Kennedy, E.M. New Zealand fossil spores and pollen: an
575 illustrated catalogue. In: GNS Science Miscellaneous Series No. 4, 4th edition.
576 http://data.gns.cri.nz/sporepollen/index.htm (2011).

67. Prebble, J. G. Descriptions and occurrences of pollen and spores from New Zealand Cenozoic sediments, *GNS Science Internal Report 2016/09*, 137 (2016).
68. Askin, R.A. Spores and pollen from the McMurdo Sound erratics, Antarctica In: Palaeobiology and Palaeoenvironments of Eocene Rocks, McMurdo Sound, East Antarctica. Antarctic Research Series v76 (Eds. Stilwel, J.D. and Feldman, R.M.), American Geophysical Union 2000 (2000).
69. Askin, R.A. and Raine, J. I. Oligocene and Early Miocene terrestrial palynology of the Cape Roberts Drillhole CRP-2/2A, Victoria Land Basin, Antarctica. *Terra Antarctica* **7**, 493-501 (2000).
70. Truswell, E.M. Recycled Cretaceous and Tertiary pollen and spores in Antarctic marine sediments: a catalogue. *Palaeontographica Abteilung B* **186**, 121-174 (1983).
71. Fensome, R. A. & Williams, G. L. The Lentin and Williams index of fossil dinoflagellates. American Association of Stratigraphic Palynologists Foundation Contribution Series 42 (2004).
72. Hannah, M. J., Wilson, G. J. & Wrenn, J. H. Oligocene and miocene marine palynomorphs from CRP-2/2A, Victoria Land Basin, Antarctica. *Terra Antarct.* **7** 503–511 (2000).
73. Hannah, M. J. The palynology of ODP site 1165, Prydz Bay, East Antarctica: a record of Miocene glacial advance and retreat. *Palaeogeogr. Palaeoclimatol. Palaeoecol.* **231,** 120–133 (2006).
74. Clowes, C. D., Hannah, M. J., Wilson, G. J. & Wrenn, J. H. Marine palynostratigraphy of the Cape Roberts Drill-holes, Victoria Land Basin, Antarctica, with descriptions of six new species of organic-walled dinoflagellate cyst. *Mar. Micropaleontol.* **126**, 65–84 (2016).
75. Bijl P., et al. Stratigraphic calibration of Oligocene–Miocene organic-walled dinoflagellate cysts from offshore Wilkes Land, East Antarctica, and a zonation proposal. *J. Micropalaeontology* **37**, 105–138 (2018). https://doi.org/10.5194/jm-37-105-2018

602 76. Benninghoff, W. S. Calculation of pollen and spores density in sediments by addition of
603 exotic pollen in known quantities. *Pollen et Spores* **6**, 332–333 (1962).
604 77. Harland, R., & Pudsey, C. J. Dinoflagellate cysts from sediment traps deployed in the
605 Bellingshausen, Weddell and Scotia seas, Antarctica. *Mar. Micropaleontol.* **37**, 77-99 (1999).
606 78. Prebble, J. G. et al. An expanded modern dinoflagellate cyst dataset for the Southwest Pacific
607 and Southern Hemisphere with environmental associations. *Mar. Micropaleontol.* **101**, 33–48
608 (2013).
609 79. Hartman, J. D., Bijl, P. K., & Sangiorgi, F. A review of the ecological affinities of marine
610 organic microfossils from a Holocene record offshore of Adélie Land (East
611 Antarctica). *Journal of Micropalaeontology* **37**, 445-497 (2018).
612 80. Zonneveld, K. A. et al. Atlas of modern dinoflagellate cyst distribution based on 2405 data
613 points. *Review of Palaeobotany and Palynology* **191**, 1-197 (2013).
614 81. Warny, S. et al. Palynomorphs from a sediment core reveal a sudden remarkably warm
615 Antarctica during the middle Miocene. *Geology* **37**, 955–958 (2009).
616 82. Sangiorgi, F., et al. Southern Ocean warming and Wilkes Land ice sheet retreat during the
617 mid-Miocene. *Nature Communications* **9**, 1-11 (2018).
618 83. Zhang, Y. G., Pagani, M., Liu, Z. H., Bohaty, S. M., & DeConto, R. M. (2013). A 40-million-
619 year history of atmospheric CO_2. *Philosophical Transactions of the Royal Society A:*
620 *Mathematical, Physical and Engineering Sciences* **371,** 20130096 (2001)
621 https://doi.org/10.1098/rsta.2013.0096
622 84. Super, J. R., Thomas, E., Pagani, M., Huber, M., O'Brien, C., & Hull, P. M. (2018). North
623 Atlantic temperature and pCO_2 coupling in the early-middle Miocene. *Geology* **46**, 519-
624 522. https://doi.org/10.1130/g40228.1

625 85. Witkowski, C. R., Weijers, J. W. H., Blais, B., Schouten, S., & Sinninghe Damsté, J.
626 S. (2018). Molecular fossils from phytoplankton reveal secular pCO_2 trend over the
627 Phanerozoic. *Science Advances* **4**, eaat4556. https://doi.org/10.1126/sciadv.aat4556
628 86. Ji, S. C., Nie, J. S., Lechler, A., Huntington, K. W., Heitmann, E. O., & Breecker, D.
629 O. (2018). A symmetrical CO_2 peak and asymmetrical climate change during the middle
630 Miocene. *Earth and Planetary Science Letters* **499**, 134 -
631 144. https://doi.org/10.1016/j.epsl.2018.07.011
632 87. Breecker, D. & Retallack, G. (2014). Refining the pedogenic carbonate atmospheric CO_2
633 proxy and application to Miocene CO_2. *Palaeogeography, Palaeoclimatology,*
634 *Palaeoecology*, **406**, 1-8. https://doi.org/10.1016/j.palaeo.2014.04.012
635 88. Pearson, P. N. & Palmer, M. R. (2000). Atmospheric carbon dioxide concentrations over the
636 past 60 million years. *Nature* **406**, 695-699. https://doi.org/10.1038/35021000
637 89. Tripati, A. K., Roberts, C. D., & Eagle, R. A. (2009). Coupling of CO_2 and Ice Sheet Stability
638 Over Major Climate Transitions of the Last 20 Million Years. *Science* **326**, 1394-
639 1397. https://doi.org/10.1126/science.1178296
640 90. Greenop, R., Foster, G. L., Wilson, P. A., & Lear, C. H. (2014). Middle Miocene climate
641 instability associated with high-amplitude CO_2 variability. *Paleoceanography* **29**, 845-
642 853. https://doi.org/10.1002/2014pa002653
643 91. Sosdian, S. M. et al. Constraining the evolution of Neogene ocean carbonate chemistry using
644 the boron isotope pH proxy**.** *Earth and Planetary Science Letters* **498**, 362-376 (2018).
645 https://doi.org/10.1016/j.epsl.2018.06.017
646 92. Londoño, L., et al. Early Miocene CO_2 estimates from a Neotropical fossil leaf assemblage
647 exceed 400 ppm. *American Journal of Botany*, **105**, 1929-1937 (2018).
648 https://doi.org/10.1002/ajb2.1187

649 93. Kürschner, W. M., Kvaček, Z., & Dilcher, D. L. (2008). The impact of Miocene atmospheric
650 carbon dioxide fluctuations on climate and the evolution of terrestrial
651 ecosystems. *Proceedings of the National Academy of Sciences* **105**, 449-
652 453. https://doi.org/10.1073/pnas.0708588105
653 94. Cui, Y., Schubert, B. A., & Jahren, A. H. A 23 m.y. record of low atmospheric
654 CO2. *Geology*, **48**, 888-892 (2020). https://doi.org/10.1130/g47681.1

655 **Acknowledgements**

656 This research used data and samples provided by the International Ocean Discovery Program
657 (IODP), which is sponsored by the US National Science Foundation (NSF) and participating
658 countries under the management of Joint Oceanographic Institutions. J.W.M. was supported by a
659 NERC studentship. Neodymium and Sr isotope analysis and U-Pb dating of detrital zircons was
660 funded through NERC UK IODP grant NE/R018219/1. Clast counts performed by L.Z., F.T. and
661 M.P. were funded by the Italian National Antarctic Research Program (PNRA - Programma
662 Nazionale Richerche in Antartide) - grant number PNRA18-00233. R.M. was supported by Royal
663 Society Te Apārangi Marsden Fund (18-VUW-089). L.F.P. has been funded by the European
664 Union's Horizon 2020 research and innovation programme under the Marie Sklodowska-Curie grant
665 agreement No. 792773 WAMSISE. D.K. was supported by the IODP JOIDES Resolution Science
666 Operator and National Science Foundation (grant 1326927). We thank B. Coles, K. Kreissing and P.
667 Simoes Pereira for technical support. Southern Transantarctic Mountain rock samples for Nd and Sr
668 isotope analysis were provided by the Polar Rock Repository with support from the National Science
669 Foundation, under Cooperative Agreement OPP-1643713.

670 **Author Contributions**

671 T.v.d.F., R.M.M, L.D.S and J.W.M. designed the research; J.W.M. conducted the Nd and Sr isotope
672 analyses; L.Z., F.T. and M.P. performed the clast counts; J.W.M., P.V. and A.C. produced the zircon

U-Pb data; F.B. and V.B.R. collected the clay mineralogy data; F.S., J.P. and C.B. performed the palynological counts and interpretations; S.H. provided the hornblende $^{40}Ar/^{39}Ar$ data; L.F.P., F.C. and L.D.S. calculated the sediment volume estimate; R.L, R.M.M., T.E.v.P., D.H., D.K.K. and E.G., helped construct and improve the age model; N.B.S and S.R.M. conducted the astrochronlogical analyses; D.K.K. provided the XRF data; J.W.M. created the figures and wrote the text with assistance from all authors.

Data availability All data from this study can be found in the Supplementary Information and have been submitted to the British Geological Survey National Geoscience Data Centre.

Competing Interests The authors declare no competing interests.

Correspondence and requests for materials should be addressed to James W. Marschalek.